

SUPPLEMENTARY INFORMATION

Combining catalysis and computational fluid dynamics towards improved process design for ethanol dehydration

Matthew E. Potter,* Lindsay-Marie Armstrong,* and Robert Raja

University of Southampton, University Road, Highfield, Southampton, SO17 1BJ, UK.

* M.E.Potter@soton.ac.uk, L.Armstrong@soton.ac.uk

Contents

Experimental details	Page S2
Catalyst synthesis	Page S2
Textural characterization	Page S2
MAS NMR	Page S2
Acid site characterization	Page S3
Catalysis procedure	Page S3
Rate constant derivation	Page S3
Textural characterization of SAPO-34	Page S4
MAS NMR spectra	Page S5
Acidity characterization	Page S7
Further catalytic data	Page S8
Computational details	Page S12
Model description	Page S12
Equations and derivations	Page S12
Full computational parameters	Page S14
Numerical computational solutions	Page S15
SI References	Page S16

Experimental details

Catalyst Synthesis

31.1 g of tetraethyl ammonium hydroxide (35 % in H₂O, Aldrich) was added to 15.1 g aluminium isopropoxide (Aldrich), and stirred for 90 minutes. 0.66 g of fumed silica (Aldrich) was added to the solution, stirring for a further 30 minutes. A homogeneous solution of 8.5 g of phosphoric acid (85 % in H₂O, Aldrich) in 12.2 mL of water was added to the above solution which was stirred for a 120 minutes to obtain a gel with the composition 1.0Al:1.0P:0.15:Si:1.0TEAOH:50H₂O.

The gel was transferred to a Teflon-lined stainless-steel autoclaves, and heated to 200 °C in a pre-heated, fan-assisted oven (WF-30 Lenton), and heated at 200 °C under autogeneous pressure for 60 hr. The white solid product was collected by centrifuge, washed with approx. 100 mL deionised water, and dried in air (80 °C) overnight. The as-prepared sample was calcined in a tube furnace under a flow of air at 575 °C for 16 hr yielding a white solid.

Textural characterization

ICP analysis was performed by MEDAC. A Perkin-Elmer Optimum 3000 DV was used for ICP analyses with calcined samples prepared and fully digested in 10 mL of deionized water and 10 mL of ACS Plus Certified H₂SO₄ (Fisher Scientific). Solutions of standard concentrations were used for calibration.

Phase purity and crystallinity of materials was confirmed by powder X-ray diffraction. Powder X-ray diffraction (PXD) was carried out using a Bruker D2 Phaser diffractometer using Cu K_{α1}/K_{α2} radiation $\lambda = 1.5418 \text{ \AA}$, PXD patterns were run over a 2 θ range of 5-45° with a scan speed of 3° min⁻¹ and increment of 0.01°.

BET surface area measurements were performed on a sample dried under 20 mTorr of vacuum at 120°C overnight. Analysis was performed on a Micromeritics Gemini 2375 surface area analyzer.

Scanning electron microscopy images were obtained using a JOEL-JSM5910 microscope with accelerating voltage of 0.3-30 kV. The samples were prepared by carbon coating.

MAS NMR

All NMR measurements were performed on a Chemagnetics Infinity 400 spectrometer on a 4 mm MAS double-resonance APEX probe. For all samples, approximately 100 mg of material was quickly transferred in a thin wall zirconium oxide rotor and then spun at 8 kHz using compressed nitrogen, in order to prevent sample degradation in air, for bearing, drive and purge. The nitrogen gas was generated in-house from evaporation of liquid nitrogen in high pressure 1300 L tanks suitably connected to the NMR facility. ²⁷Al NMR experiments were performed using direct acquisition (128 scans with a pulse delay of 2 s between scans). ³¹P NMR data were acquired with direct acquisition (4 scans and 120 s delay between scans). ²⁹Si NMR data for all 1D experiments were performed using cross-polarization and SPINAL64 decoupling.^[1] Typical spectra were acquired with 8192 scans and 2 s between scans. The chemical shift axes in the ²⁷Al, ³¹P and ²⁹Si spectra were referenced using 1M AlCl₃ aqueous solution (0 ppm), 85 % H₃PO₄

(0 ppm) and silicon rubber (-22.42 ppm) respectively, following the convention described in reference 5. The NMR data was processed using matNMR.

Acid site characterization

CO-probed FT-IR experiments were performed in a custom designed IR flow cell that allowed for sample heating and cryogenic cooling. Freshly calcined samples were ground and pressed into 13 mm diameter self-supporting pellets (~8 mg/cm²) and heated at 10 °C/min to 550 °C in a mixture of 20 % O₂ in N₂ [Matheson UHP grade further purified using a P400 air purifier(VICI)] and held for 1 h. The flow was then switched to helium [Matheson UHP grade further purified using a P-100 helium purifier(VICI) and an indicating OMI-1 purifier(Supelco)] and held for an additional hour. The system was then cooled to ~-175°C and a spectrum recorded. Nine 0.02 cm³ injections of CO (Matheson research purity) were added to the system followed by a final injection of 0.20 cm³. After each injection, the system was equilibrated for 3 min and a spectrum recorded.

TPD measurements were performed on a custom built system using TCD detectors to monitor ammonia concentration. As-synthesized materials were pretreated by heating at 10 °C/min to 550 °C in a 20 % O₂/helium mixture [Matheson UHP grade passed through a Drierite/molecular sieve gas purifier (Alltech Associates)] and held for 2 h. The samples were exposed to ammonia and allowed to equilibrate at 150 °C for 8 h. Desorption was performed in flowing helium [Matheson UHP grade further purified with an Oxy-Trap (Alltech Associates) and an indicating OMI-1 purifier (Supelco)] at 10 °C/min to 600 °C and held for 40 minutes at 600 °C.

Catalysis procedure

Catalysis was performed using a custom build flow reactor provided by Cambridge Reactor Design. The reactor comprised of a syringe pump, laptop computer, two mass flow controllers, and reactor with heater and control box. A 224 mm quartz reactor tube (4 mm id, 6 mm od) with a 4 mm high frit 80 mm from the base of the tube and a gas inlet 25.8 mm from the top was placed inside the heater jacket. Liquid and gas flows were controlled using a Harvard Apparatus Model 33 MA1-55-3333 syringe pump and Brooks IOM585OS mass flow controller respectively and flow rates were input via computer interface.

The output was vaporized and 5 µl samples were injected as a gas into a Varian Star 3400CX gas chromatogram with flame ionization detector (FID). Samples were injected into a Perkin Elmer a HP1 cross linked methylsiloxane (30 m x 0.32 mm x 1 µm film thickness) column. All results shown are the average of two consistent samples.

Rate constant derivation

Typically kinetics is performed on batch processes. The reaction is sampled as a function of time, where other conditions are constant. In this continuous flow process we vary the flow rate, and consequently the contact time of the substrate to achieve the same effect. This has the caveat of also varying the

concentration of the substrate for each sample. To overcome this we have treated each set of data (at a particular WHSV/flow rate and temperature) as an individual isolated batch reaction, and then averaged the rate constants over the WHSV range, thus generating a rate constant for each of the individual pathways at each temperature.

- A) Ethanol \rightarrow Ethylene + H₂O
- B) 2Ethanol \rightarrow Diethyl Ether + H₂O
- C) Diethyl Ether \rightarrow Ethylene + Ethanol

From literature we have taken the rate constants of reactions b and c to be second order with respect to the reactant, and reaction a to be first order.^[2,3]

Textural characterization of SAPO-34

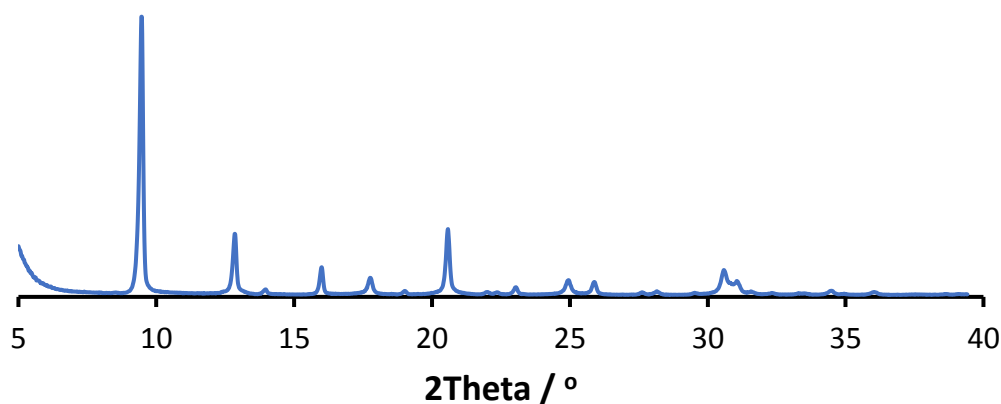


Figure S1: Powder XRD pattern showing the phase purity and crystallinity of SAPO-34.

Table S1: Optimized unit cell parameters for SAPO-34, assuming a P1 space group and metal loadings determined from ICP-MS.

Material	a / Å	b / Å	c / Å	α / °	β / °	γ / °
SAPO-34	13.72	13.77	15.01	88.13	90.42	119.77

Material	Al / wt%	P / wt%	Si / wt%
SAPO-34	23.1	20.8	3.4

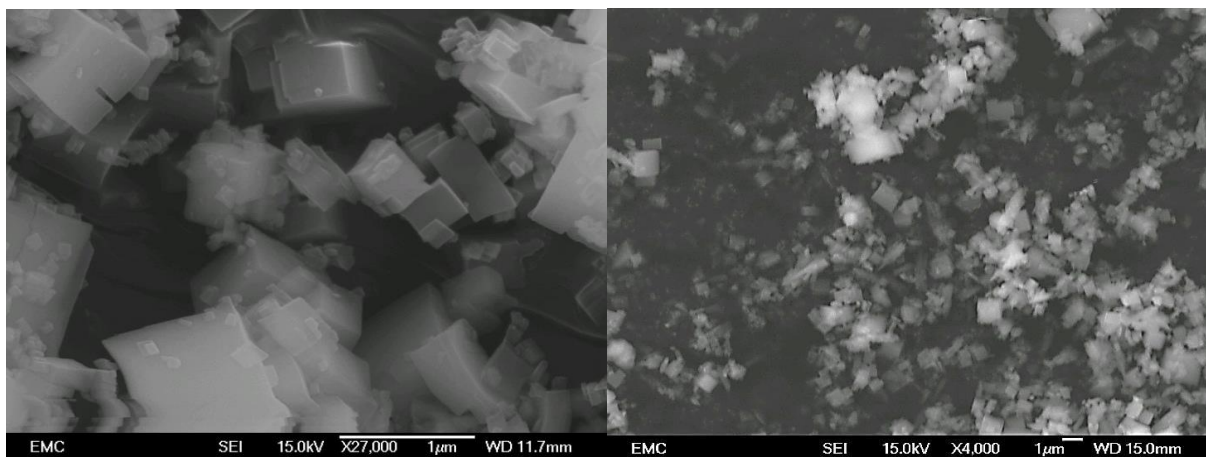


Figure S2: SEM images of SAPO-34 showing cubes of roughly 1 μm in size.

MAS NMR spectra

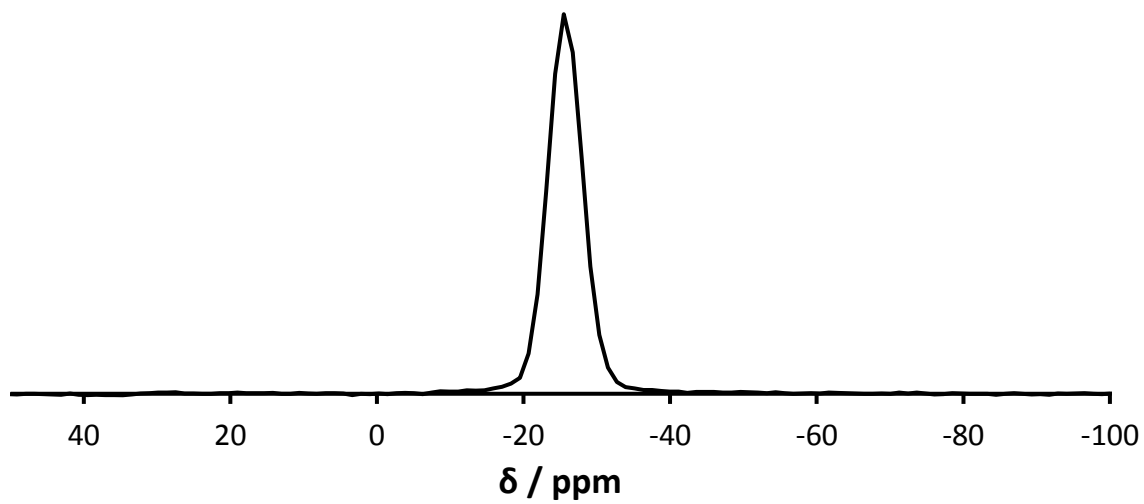


Figure S3: ^{31}P MAS NMR spectra of SAPO-34 showing a solitary peak at -26 ppm, corresponding to $\text{P}(\text{OAl})_4$.

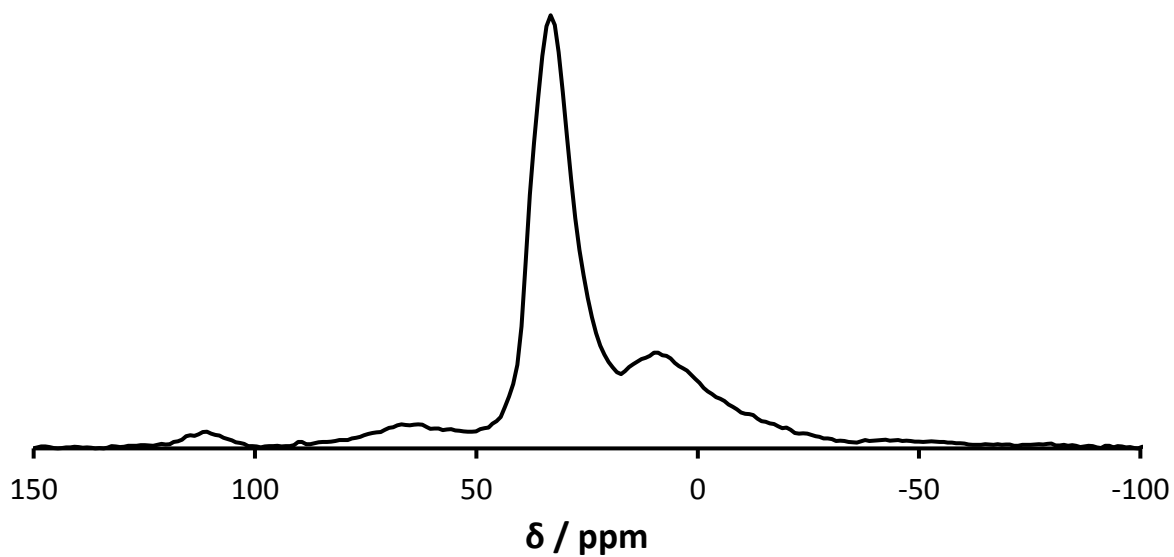


Figure S4: ^{27}Al MAS NMR spectra of SAPO-34, showing a primary peak at -33 ppm, corresponding to $\text{Al}(\text{OP})_4$, and a secondary peak at 8 ppm, corresponding to $\text{Al}(\text{OP})_4(\text{H}_2\text{O})$

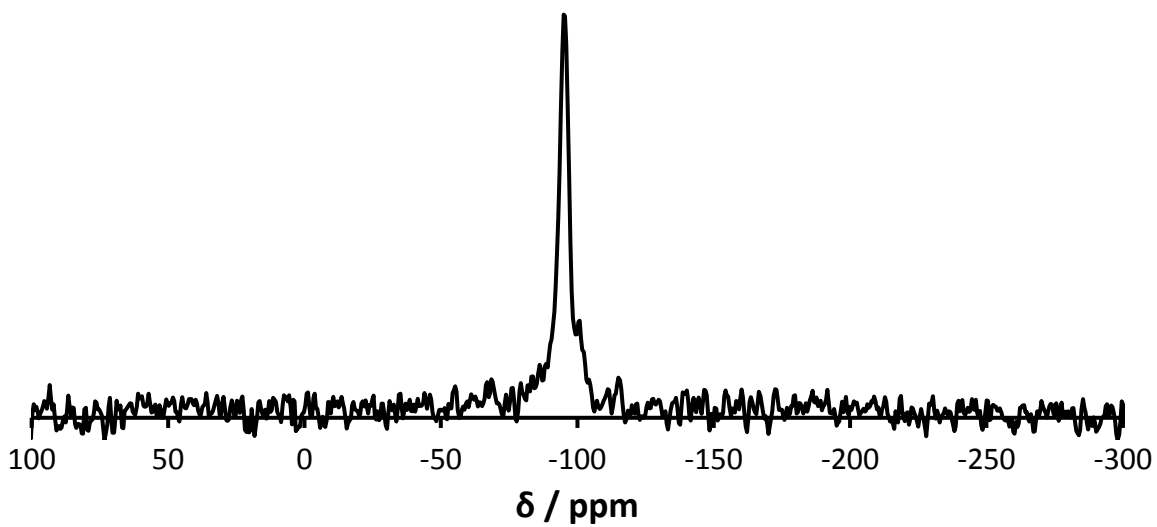


Figure S5: ^{29}Si MAS NMR showing a primary peak at -95 ppm ($\text{Si}(\text{OAl})_4$), but also smaller peaks at -103 and -115 ppm, caused by silicon islanding in the structure.

Acidity characterization

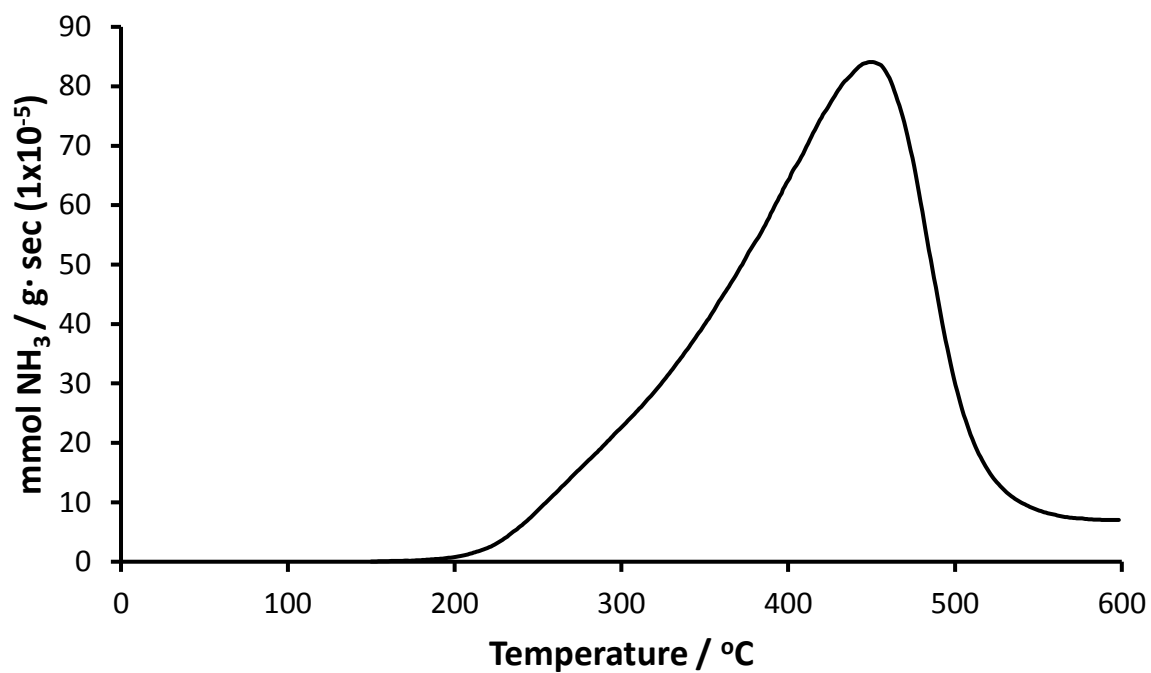


Figure S6: NH₃-TPD spectra showing the acidity of SAPO-34.

Table S2: Analysis of the NH₃-TPD of SAPO-34 showing total acidity.

Material	Peak area / (mmol g ⁻¹)						Peak maximum
	150 – 200	200 – 300	300 – 400	400 – 500	500 – 600	Total	
SAPO-34	0.0008	0.0602	0.2533	0.4268	0.0811	0.82	447

Further catalytic data

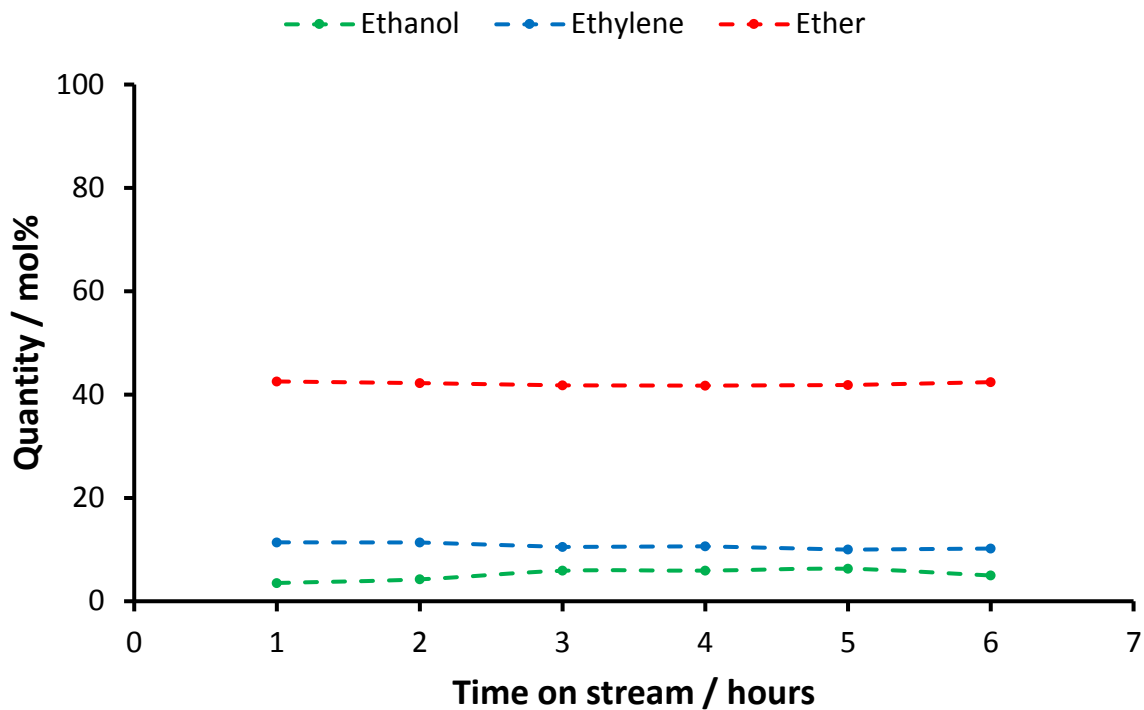


Figure S7: Time on stream study of ethanol dehydration with SAPO-34 at 200 °C, WHSV = 2.0, 25 ml/min of Helium carrier gas, showing no notable change in distribution over 6 hours.

Table S3: Rate constants and error mean and standard deviation for the individual WHSV cases at different temperature for the three possible reaction steps.

Rate constants for individual WHSVs							
185 °C	0.5	0.75	1	1.25	1.5	1.75	2
k_a	7.67E-05	9.17E-05	1.05E-04	1.05E-04	1.07E-04	1.12E-04	1.05E-04
k_b	5.55E+02	5.34E+02	5.55E+02	5.25E+02	4.90E+02	5.32E+02	4.46E+02
k_c	7.89E+00	8.40E+00	1.11E+01	1.24E+01	1.53E+01	1.28E+01	1.13E+01
Error mean	-7.911e-16	-9.999e-10	-2.500e-9	-2.667e-9	-8.332e-11	-4.167e-10	1.583e-9
Error Std. Dev.	8.792e-15	5.774e-10	1.443e-9	1.748e-9	2.100e-9	1.382e-9	1.382e-9
200 °C							
k_a	1.52E-04	1.50E-04	1.86E-04	2.28E-04	2.05E-04	1.39E-04	2.21E-04
k_b	1.12E+03	1.18E+03	1.09E+03	1.02E+03	1.12E+03	1.01E+03	1.04E+03
k_c	7.54E+01	6.77E+01	6.12E+01	4.95E+01	4.85E+01	5.19E+01	4.33E+01
Error mean	-5.000e-10	-1.417e-9	1.333e-9	-2.667e-9	-5.833e-10	-8.333e-10	-1.417e-9
Error Std. Dev.	1.118e-9	1.847e-9	1.748e-9	1.748e-9	1.754e-9	3.727e-10	6.401e-10
215 °C							
k_a	2.05E-04	3.14E-04	2.35E-04	5.01E-04	3.39E-04	4.07E-04	3.02E-04
k_b	1.67E+03	1.67E+03	1.65E+03	1.62E+03	1.54E+03	1.64E+03	1.57E+03
k_c	3.26E+02	2.39E+02	2.46E+02	1.53E+02	1.35E+02	1.18E+02	1.30E+02
Error mean	5.833e-10	-1.333e-9	-5.833e-10	-2.750e-9	8.333e-10	-1.583e-9	1.583e-9
Error Std. Dev.	1.754e-9	2.095e-9	2.842e-9	1.588e-9	2.764e-9	2.564e-9	2.564e-9
230 °C							
k_a	4.16E-04	3.64E-04	2.73E-04	9.06E-04	4.15E-04	5.75E-04	5.22E-04
k_b	2.56E+03	2.53E+03	2.53E+03	2.40E+03	2.30E+03	2.35E+03	2.44E+03
k_c	2.66E+03	1.27E+03	1.05E+03	6.08E+02	5.48E+02	3.91E+02	3.20E+02
Error mean	-6.667e-10	-1.500e-9	9.170e-10	-3.333e-10	-1.750e-9	-6.667e-10	7.500e-10
Error Std. Dev.	2.392e-9	8.660e-10	7.592e-10	7.453e-10	1.010e-9	3.300e-9	4.330e-10

*Note: WHSV has units of hr^{-1} , units for k_a are s^{-1} , due to the first order nature of the reaction. k_b and k_c are in units of $\text{ml mol}^{-1} \text{s}^{-1}$ as they are represent second order reactions.

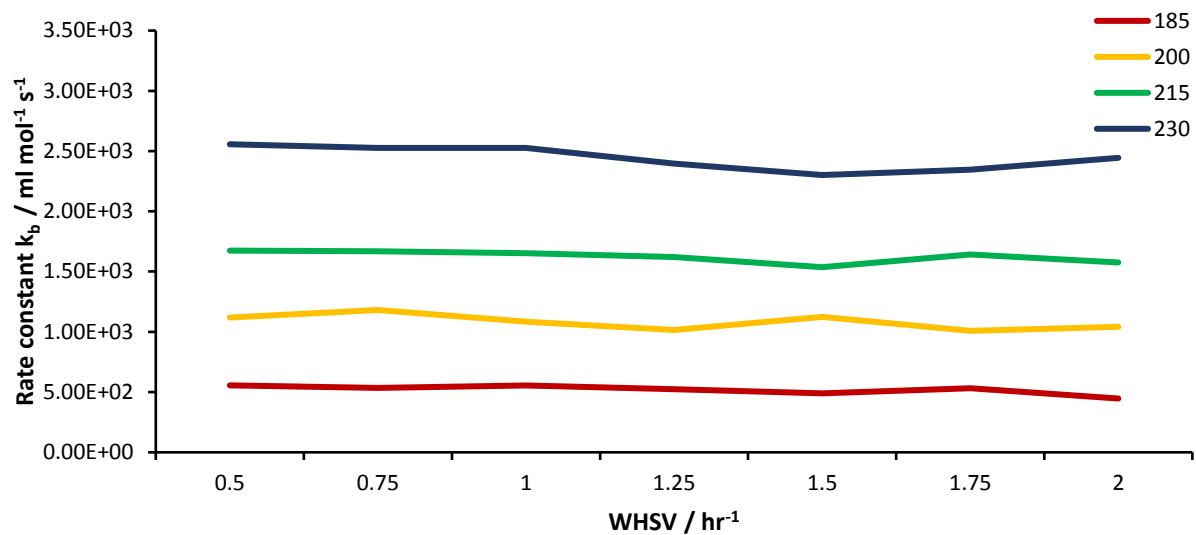


Figure S8: Kinetic rate constants of reaction b for varying WHSVs over different temperatures shown in °C.

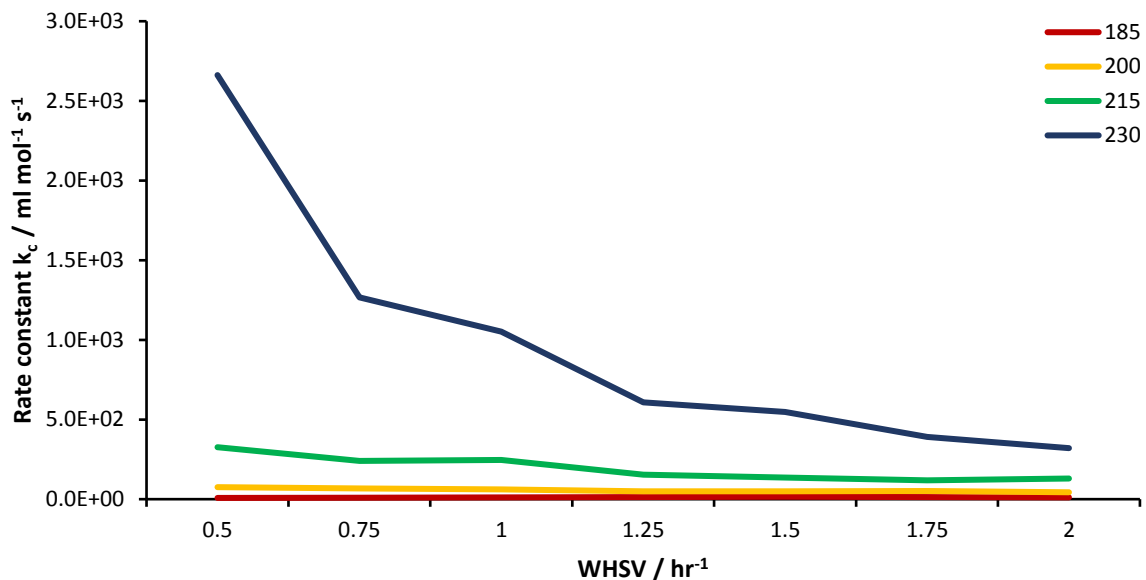


Figure S9: Kinetic rate constants of reaction c for varying WHSVs over different temperatures shown in °C.

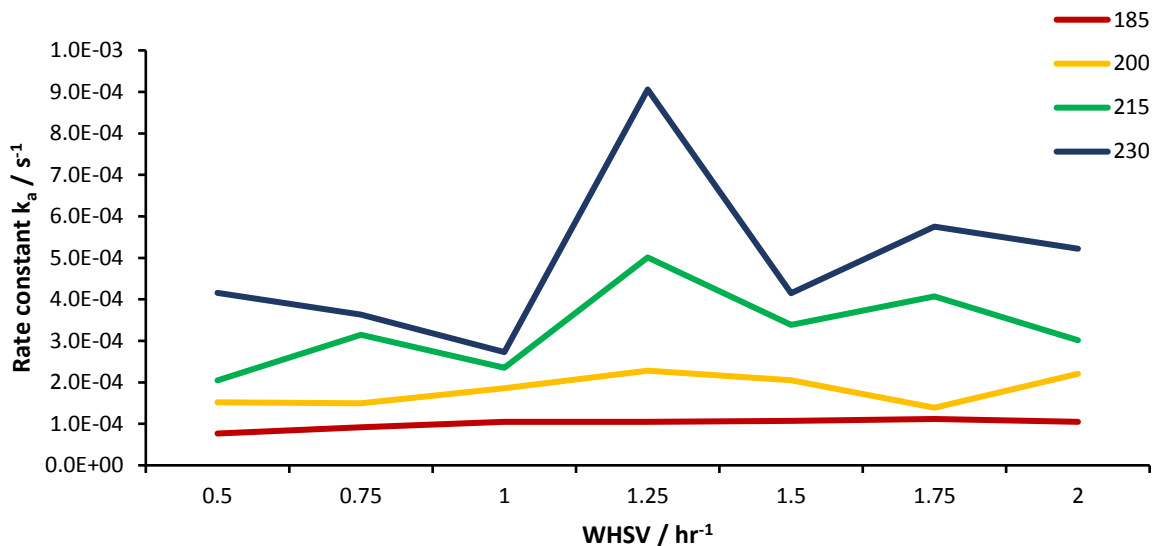


Figure S10: Kinetic rate constants of reaction a for varying WHSVs over different temperatures shown in °C.

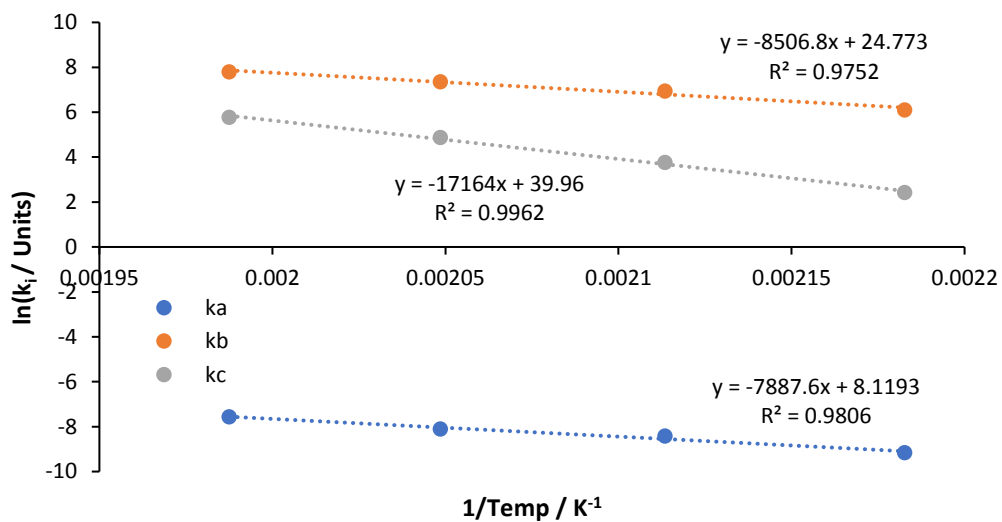


Figure S11: Arrhenius plot of the calculated average rate constants to derive the activation energy. Note units of k vary, they are s^{-1} for k_a , and $ml\ mol^{-1}\ s^{-1}$ for k_b and k_c .

Computational details

Model description

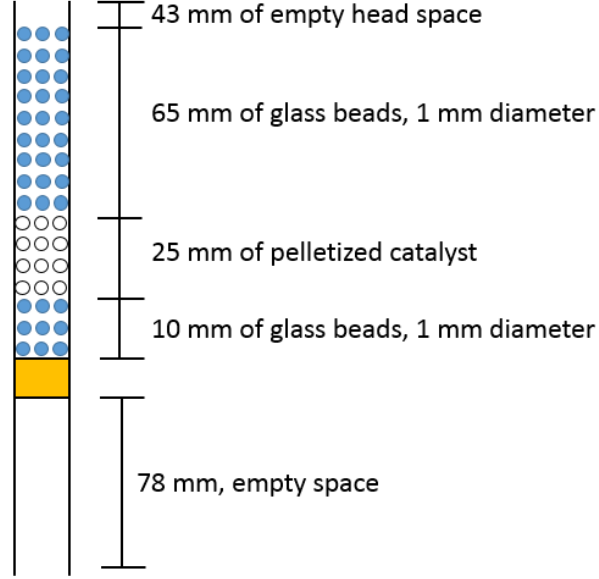


Figure S12: Experimental set-up with an internal and external diameter of 4 mm and 6 mm, respectively

Equations and derivations

The standard equation and momentum equations, as described by Batchelor,^[4] were modified to include a porosity factor, ε , to account for the porosity of the pelletized bed as follows:^[5]

$$\frac{\partial}{\partial t}(\varepsilon\rho_f) + \nabla \cdot (\varepsilon\rho_f\vec{v}) = 0, \quad (3)$$

$$\frac{\partial}{\partial t}(\varepsilon\rho_f\vec{v}) + \nabla \cdot (\varepsilon\rho_f\vec{v}\vec{v}) = -\varepsilon\nabla P + \nabla \cdot \left(\varepsilon\mu \left[(\nabla\vec{v} + \nabla\vec{v}^T) - \frac{2}{3}\nabla \cdot \vec{v}\mathbf{I} \right] \right) + S_i, \quad (4)$$

Where, ρ_f is the density of the mixture gas, \vec{v} is the velocity vector, μ is the dynamic viscosity. Empirically determined flow resistance was applied to the pelletized catalytic region in the form of the Darcy-Forcheimer Law^[5,6] which accounts for the viscous and inertial losses experienced in a packed pellet bed:

$$S_i = -\left(\frac{\mu}{\alpha}\vec{v} + \frac{1}{2}C_2\rho_f\vec{v}\vec{v} \right), \quad (5)$$

Where α is the permeability, and C_2 is the inertial resistance factor.

The source term subsequently creates a pressure drop (ΔP) along the length of the bed (L):

$$\frac{\Delta P}{L} = -\left(\frac{\mu}{\alpha}\vec{v} + \frac{1}{2}C_2\rho_f\vec{v}\vec{v} \right). \quad (6)$$

The semi-empirical Ergun equation, given in Eqn (7), is commonly used for ascertaining the pressure drops in packed beds:^[7]

$$\frac{\Delta P}{L} = \frac{150(1-\varepsilon)^2}{D_p^2 \varepsilon^3} \mu \vec{v} + \frac{1.75(1-\varepsilon)}{D_p \varepsilon^3} \rho \vec{v} \vec{v}. \quad (7)$$

Comparison of Eqn (6) & (7) produces expressions for the permeability and inertial resistance, respectively:

$$\frac{1}{\alpha} = \frac{150(1-\varepsilon)^2}{D_p^2 \varepsilon^3}, \quad (8)$$

$$C_2 = \frac{3.5(1-\varepsilon)}{D_p \varepsilon^3}. \quad (9)$$

The conservation of species transport is accounted for by solving the following equation:

$$\frac{\partial}{\partial t} (\varepsilon \rho_f Y_i) + \nabla \cdot (\rho_f \vec{v} Y_i) = -\nabla \cdot \vec{J}_i + R_i, \quad (10)$$

where Y_i represents the local mass fraction of individual species. R_i is the rate of individual species production as a result of the chemical reactions. The reaction kinetics for these reactions will be determined experimentally in the next section for implementation into the model. The diffusion of species, \vec{J}_i , due to concentration gradients is defined as:

$$\vec{J}_i = -\rho_f D_{i,m} \nabla Y_i, \quad (11)$$

where $D_{i,m}$ is the diffusion coefficient for each species.

The evolution of the temperature field is obtained by solving the following energy equation,

$$\frac{\partial}{\partial t} (\varepsilon \rho_f E_f + (1-\varepsilon) \rho_s E_s) + \nabla \cdot ((\rho_f E_f + P) \vec{v}) = \nabla \cdot (k_{eff} \nabla T) + S_f \quad (12)$$

where E_f and E_s represent the total fluid and solid energy, respectively, T is temperature, ρ_s is the pellet density and S_f the temperature change due to reactions. The effective thermal conductivity is given by:

$$k_{eff} = \varepsilon k_f + (1-\varepsilon) k_s. \quad (13)$$

Full computational parameters

Table S4: Simulated mass flow rate inlet values for different WHSV cases.

Weight Hourly Space Velocity (WHSV) / hr ⁻¹	Ethanol / (g s ⁻¹)	Heptane / (g s ⁻¹)	Helium / (g s ⁻¹)
0.5	3.73093E-05	4.14548E-06	0.00006875
0.75	5.59639E-05	6.21822E-06	0.00006875
1	7.46186E-05	8.29095E-06	0.00006875
1.25	9.32732E-05	1.03637E-05	0.00006875
1.5	0.000111928	1.24364E-05	0.00006875
1.75	0.000130583	1.45092E-05	0.00006875
2	0.000149237	1.65819E-05	0.00006875

Table S5: Simulated cases for varying temperature and varying WHSVs.

Geometric parameters	Value		Dimensions
Reactor diameter	0.004		[m]
Reactor height	0.025		[m]
Average pellet diameter, D_p	1×10^{-6}		[m]
Porosity, ϵ	0.44		[-]
Viscous resistance, $1/\alpha$	5.54×10^{14}		[m ⁻²]
Inertial resistance, C_2	2.31×10^7		[m ⁻¹]
Pore surface-to-volume ratio	1.76×10^9		[m ⁻¹]
Species Parameters	Density, ρ_{fi} / kg m ⁻³	Enthalpy, ΔH_i / kJ mol ⁻¹	Entropy, S^\ominus / J mol ⁻¹ K ⁻¹
Water, H ₂ O	0.5542	-241.83	188.84
Ethanol, C ₂ H ₅ OH	2.06	-235.3	283
Ethylene, C ₂ H ₄	1.137	52.47	219.32
Diethyl ether, C ₄ H ₁₀ O	3.185	-252.7	342.2
Helium, He	0.1625	0	126.03
Heptane, C ₇ H ₁₆	4.25	-187.8	428.01
Varying parameters	Value		Dimensions
Temperature	185, 200, 215, 230		[°C]
Weight hourly space velocities	0.5, 0.75, 1.0, 1.25, 1.5, 1.75, 2.0		[hr ⁻¹]

Table S6: Simulated cases for varying temperature and varying WHSVs.

Case	Temperature / °C	WHSV / hr ⁻¹
1	185	2.00
2	200	2.00
3	215	2.00
4	230	2.00
5	200	0.5
6	200	0.75
7	200	1.00
8	200	1.50
9	200	1.75
9	200	2.00

Numerical computational solutions

Table S7: Exiting molar concentrations and mole fractions for 2.0 WHSV (1/hr) at varying temperatures

		Molar concentration / mol ml ⁻¹				Mole fractions			
		C ₂ H ₅ OH	C ₂ H ₄	C ₄ H ₁₀ O	H ₂ O	C ₂ H ₅ OH	C ₂ H ₄	C ₄ H ₁₀ O	H ₂ O
185 °C	Computational	7.56E-07	2.91E-07	2.67E-06	2.96E-06	11.3	4.4	40.0	44.3
	Experimental	7.13E-07	4.22E-07	3.37E-06	3.79E-06	8.6	5.1	40.6	45.7
200 °C	Computational	3.83E-07	7.61E-07	2.54E-06	3.30E-06	5.5	10.9	36.4	47.3
	Experimental	4.75E-07	9.72E-07	3.22E-06	4.19E-06	5.4	11.0	36.3	47.3
215 °C	Computational	4.00E-07	1.59E-06	2.04E-06	3.64E-06	5.2	20.8	26.6	47.4
	Experimental	5.27E-07	2.02E-06	2.66E-06	4.69E-06	5.3	20.4	27.0	47.3
230 °C	Computational	3.38E-07	2.85E-06	1.33E-06	4.17E-06	3.9	32.8	15.3	48.1
	Experimental	4.77E-07	3.54E-06	1.93E-06	5.47E-06	4.2	31.0	16.9	47.9

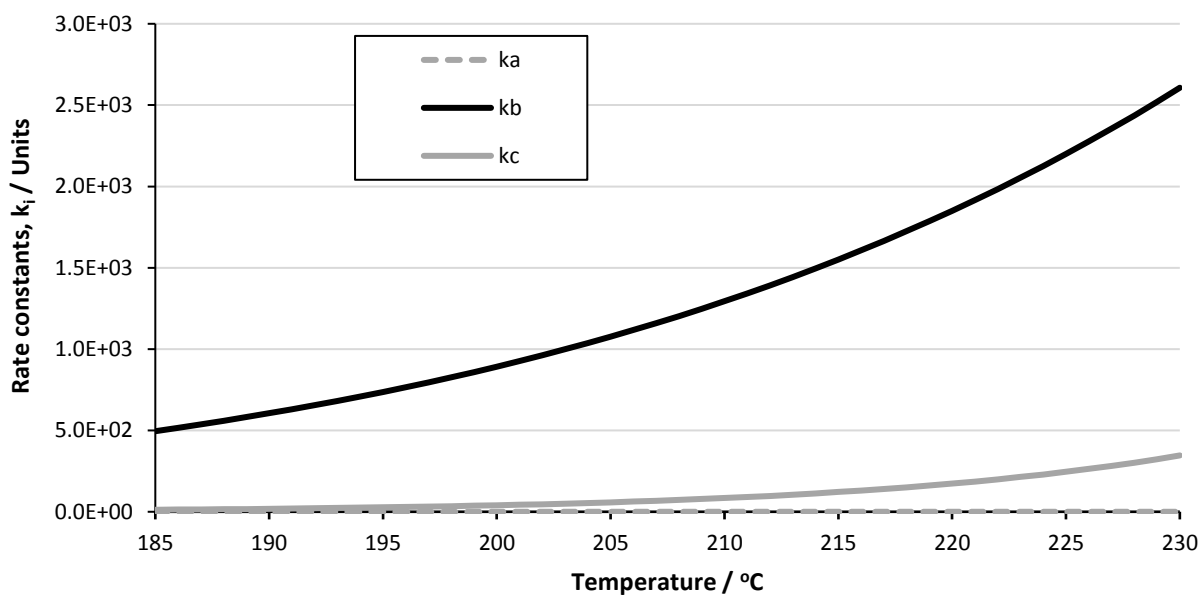


Figure S13: Variation in rate constant values for the three steps with temperature. Units of k vary with k_a being in s^{-1} , while k_b and k_c are in $ml\ mol^{-1}\ s^{-1}$.

Table S8: Exiting concentrations (mol/ml) and mole fractions for varying WHSV at 200 and 230 °C.

			Concentration / mol ml ⁻¹				Mole fractions				
			C ₂ H ₅ OH	C ₂ H ₄	C ₄ H ₁₀ O	H ₂ O	C ₂ H ₅ OH	C ₂ H ₄	C ₄ H ₁₀ O	H ₂ O	
200 °C	0.5	Computational	9.78E-08	2.52E-07	7.29E-07	9.81E-07	4.7	12.2	35.4	47.6	
		Experimental	1.07E-07	4.36E-07	6.70E-07	1.11E-06	4.6	18.8	28.9	47.7	
	0.75	Computational	1.46E-07	3.59E-07	1.07E-06	1.43E-06	4.9	12.0	35.6	47.6	
		Experimental	1.69E-07	5.32E-07	1.06E-06	1.59E-06	5.0	15.8	31.6	47.5	
	1.0	Computational	1.94E-07	4.56E-07	1.39E-06	1.85E-06	5.0	11.7	35.8	47.5	
		Experimental	2.27E-07	6.63E-07	1.44E-06	1.74E-06	5.1	15.0	32.5	47.4	
	1.25	Computational	2.41E-07	5.44E-07	1.70E-06	2.24E-06	5.1	11.5	35.9	47.4	
		Experimental	2.78E-07	7.45E-07	1.84E-06	2.59E-06	5.1	13.7	33.8	47.4	
	1.5	Computational	2.89E-07	6.23E-07	1.99E-06	2.62E-06	5.2	11.3	36.1	47.4	
		Experimental	3.29E-07	7.89E-07	2.27E-06	3.06E-06	5.1	12.2	35.2	47.4	
	1.75	Computational	3.36E-07	6.95E-07	2.27E-06	2.97E-06	5.4	11.1	36.2	47.3	
		Experimental	4.43E-07	8.33E-07	2.66E-06	3.49E-06	6.0	11.2	35.8	47.0	
	2.00	Computational	3.83E-07	7.61E-07	2.54E-06	3.30E-06	5.5	10.9	36.4	47.3	
		Experimental	4.75E-07	9.72E-07	3.22E-06	4.19E-06	5.4	11.0	36.3	47.3	
	230 °C	0.5	Computational	7.14E-08	9.87E-07	3.55E-07	1.34E-06	2.6	35.8	12.9	48.7
			Experimental	6.20E-08	1.70E-06	1.03E-07	1.81E-06	1.7	46.4	2.8	49.2
0.75		Computational	1.06E-07	1.40E-06	5.25E-07	1.93E-06	2.7	35.4	13.3	48.7	
		Experimental	1.46E-07	2.19E-06	3.10E-07	2.50E-06	2.8	42.6	6.0	48.6	
1.0		Computational	1.39E-07	1.77E-06	6.92E-07	2.46E-06	2.8	35.0	13.7	48.6	
		Experimental	1.46E-07	2.19E-06	3.10E-07	2.50E-06	3.5	40.7	7.5	48.2	
1.25		Computational	1.72E-07	2.10E-06	8.54E-07	2.96E-06	2.8	34.5	14.0	48.6	
		Experimental	2.24E-07	3.16E-06	7.68E-07	3.93E-06	2.8	39.1	9.5	48.6	
1.5		Computational	2.04E-07	2.40E-06	1.01E-06	3.41E-06	2.9	34.1	14.4	48.5	
		Experimental	3.77E-07	3.32E-06	1.11E-06	4.43E-06	4.1	36.0	12.0	48.0	
1.75		Computational	2.35E-07	2.67E-06	1.17E-06	3.84E-06	3.0	33.8	14.8	48.5	
		Experimental	4.16E-07	3.45E-06	1.51E-06	4.97E-06	4.0	33.4	14.6	48.0	
2.00		Computational	3.38E-07	2.85E-06	1.33E-06	4.17E-06	3.9	32.8	15.3	48.1	
		Experimental	4.77E-07	3.54E-06	1.93E-06	5.47E-06	4.2	31.0	16.9	47.9	

SI References:

- [1] B. M. Fung, A. K. Khitrin and K. Ermolaev, *J. Magn. Reson.*, 2000, **142**, 97.
- [2] M. Zhang and Y. Yu, *Ind. Eng. Chem. Res.*, 2013, **52**, 9505.
- [3] V. V. Bokade and G. D. Yadav, *Applied Clay Sci.*, 2011, **53**, 263.
- [4] G. K. Batchelor, *An Introduction to Fluid Dynamics*. Cambridge Univ. Press. Cambridge, England, 1967.
- [5] J. Bear, *Dynamics of Fluids in Porous Media*. Dover, New York, 1972.
- [6] P. Forchheimer, *Zeit. Ver. Deut. Ing.*, 1901, **45**, 1781.
- [7] S. Ergun, *Chem. Eng. Prog.*, 1952, **48**, 89.